

Vehicle-Integrated Photovoltaics Irradiation Modeling Using Aerial-Based LIDAR Data and Validation with Trip Measurements

Evgenii Sovetkin,* Jonas Noll, Neel Patel, Andreas Gerber, and Bart E. Pieters

Herein, a benchmark dataset for vehicle-integrated photovoltaics irradiance modeling is proposed. The vehicle trip data consist of trips in the state of North Rhine-Westphalia in Germany starting from March 2021, which amounts to more than 73 h and a total distance of 3422 km. The sensor box is equipped with GPS, a magnetic compass, acoustic wind, and irradiance sensors and records at a rate of 0.58 Hz. The irradiance sensors are positioned on four sides of the vehicle: roof, left, right, and rear. In addition to the data, a model that uses high-resolution aerial-measured topography (LIDAR) and low-resolution satellite-based weather data to forecast the effective irradiation of modules mounted on a moving vehicle is discussed. The utility of the simulation approach is demonstrated by computing irradiation over long periods for various driving profiles and comparing results with the collected measurement data. The data are published as a challenge, and the developed software is available in open source.

1. Introduction

Recently, an increasing number of integrated photovoltaic (PV) applications appeared.^[1–3] The local environment in such applications plays a significant role in PV modules' performance, as modules are no longer unobstructed from the sky dome. The vehicle-integrated PV (VIPV) is one such application. PV modules are installed on the car's roof, sides, hood, or trunk. The captured solar energy then contributes to vehicle motion and reduces the frequency of grid charging.

Several commercial VIPV products already exist on the market. "Toyota Prius PHEV", "Hyundai Sonata", and "Hyundai Ioniq 5" are examples of mass-produced vehicles with integrated PV modules. In addition, two start-up companies, "Lightyear"^[4]

and "Sono Motors",^[5] feature integrated PV of near or above one kWp capacity.

The academic works focus on various aspects of adopting the VIPV technology. Generally, many studies argue the potential benefits of the VIPV. Kanz et al.^[6] perform a life-cycle assessment study, simulating the performance of a delivery van with VIPV for 8 years in Cologne, Germany, thus showing the benefits of PV and the adverse effects of shading on vehicle performance. Heinrich et al.^[7] estimate the expected solar range of different VIPV setups for an average year in Freiburg, Germany, showing that VIPV could theoretically cover the typical driving distance. Sierra et al.^[8] design a study on conceptual PV applications for electric mobility systems, revealing several challenges, such


as package requirements and charging technologies. Yamaguchi et al.^[9,10] present a general outlook on different technologies in VIPV, their conversion efficiency impact on reduction in CO₂ emission, and increase in driving range of the electric-based vehicles. They argue that most family cars in Japan can run only by sunlight without supplying fossil fuels. However, even general studies indicate that the local environment and general vehicle location play a significant role in VIPV performance. Thiel et al.^[11] reveal that the grid power needed to drive such vehicles on identical routes can vary by more than 44% between climates.

Peibst et al.^[12] build a practical electrically driven, commercial demonstration vehicle with integrated PVs. The demonstrator vehicle has irradiation, wind, temperature, and magnetic and global positioning sensors. Peibst et al. report the range extension of 36 km on a test route.

VIPV modules need to adapt to the shape of a car, and therefore they are curved. For example, Neven-du Mont et al.^[13] show that the roof's curvature decreases the yield by up to 25% when using the series interconnection of cells. To mitigate this problem, they propose the adaptation of the interconnection topology to the curvature; this is achieved by dividing the module into parallel subgroups containing cells with similar azimuth and elevation angles toward the sun. Another work^[14,15] introduces the curve correction factor to model the irradiance of a curved PV module. Based on the 1 year measurement data, Ota et al.^[15] report the correction factor of 0.92, implying the 8% loss in performance due to the roof's geometry.

VIPV modules are also exposed to significant temperature changes, as a vehicle absorbs heat when parked and cools down

E. Sovetkin, J. Noll, N. Patel, A. Gerber, B. E. Pieters
IEK-5 Photovoltaics
Forschungszentrum Jülich
52425 Jülich, Germany
E-mail: e.sovetkin@fz-juelich.de

 The ORCID identification number(s) for the author(s) of this article can be found under <https://doi.org/10.1002/solr.202200593>.

© 2022 The Authors. Solar RRL published by Wiley-VCH GmbH. This is an open access article under the terms of the Creative Commons Attribution-NonCommercial-NoDerivs License, which permits use and distribution in any medium, provided the original work is properly cited, the use is non-commercial and no modifications or adaptations are made.

DOI: 10.1002/solr.202200593

during movement. Addressing this problem, Kolhe et al.^[16] collect temperature data for five July days in Edinburgh, UK. They use an 80 Wp PV module to manage the cabin heat of a small parked electric car.

The main challenge in VIPV comes from the effects of the local environment on the modules' performance. Tomita et al.^[17] investigate the impact of partial shading and propose a distributed maximum power point (MPP) tracking to mitigate the losses caused by partial shading. Their study is verified by the experiment performed on a sunny day in June on a VIPV-equipped light van. Wetzel et al.^[18] use three high-frequency pyranometers (up to 1 kHz) to record irradiation along a 21 km track in Hanover and study its impact on the MPP tracker design. Their findings indicate that irradiance changes predominately occur at frequencies below 1 Hz; however, changes with 100 Hz can occur in certain situations, often during sunny weather. Araki et al.^[14,19] model solar irradiance by a random distribution of shading objects and car orientation with the correction of the curved surface of the PV modules. Araki et al.^[14] also perform year-long experimental measurements on a vehicle using multiple pyranometers. We compare our and^[14] experiment setups in Section 2.2. De Jong et al.^[20] analyzed the PV potential of the Dutch inland shipping fleet. They implement an irradiance and temperature model and validate it with the measurement sensor data collected on a boat. Their findings indicate that a specific energy yield of the vessels' fleet can be approximated with the Weibull distribution, with parameters depending on particular climate and topography roughness. Previous studies^[21,22] use the proprietary ArcGIS software to model irradiation for vehicles in Lisbon, Portugal. Section 3 compares our modeling approach with refs. [14,20,22].

Several projects aim to collect measurement data.^[23,24] Their solutions can be potentially scaled up to many users with different driving profiles, yielding a unique dataset and assisting in building accurate irradiance models. We compare these data loggers with ours in Section 2.

Despite this progress, we argue that the question of the accurate irradiance and yield modeling for VIPV remains open. At the same time, precise irradiance modeling is essential in yield simulations for VIPV, allowing proper investment planning and facilitating global adaptation of the VIPV technology. Furthermore, simulations are crucial for designing different VIPV subsystems, such as inverters, cell topology, and bypass diodes.

We believe publicly available benchmark measurement data benefits irradiance/yield modeling problems. Such a dataset allows researchers to compare their modeling approaches robustly. Unfortunately, to our knowledge, no such dataset is available.

Therefore, this article aims to achieve two goals. First, we publish a large measurement dataset. The data are published in a challenge, where a large portion is made public, and the rest is blinded and used to benchmark submitted models. Our focus is the irradiance, which allows us to eliminate PV module temperature and MPP tracker factors from modeling. Second, we implement an irradiance model. This irradiance model has some simplifications, which results in modeling errors. We validate the irradiance model with the collected measurement data and demonstrate that the model is statistically accurate, namely, it is valid

for irradiation simulations over long periods. Generally, irradiation accuracy is vital for computing the feasibility of VIPV.

Our modeling approach is implemented in several open-source tools. The Simple Sky Dome Projector (SSDP) library^[25] implements irradiance modeling. The PV-Geographic Raster Image Processor (PV-GRIP) tool^[26,27] is a distributed-computing framework that addresses a technical challenge, as VIPV modeling requires intensive geospatial data processing.

The article is organized as follows. First, we discuss our data logger setup in Section 2. There we provide the specification of our sensor box and describe the collected data and where one can find it. Then, Section 3 elaborates on our irradiance modeling approach, and Section 4 presents the simulation analysis. Finally, Section 5 concludes the article.

2. Experimental Section

Our experimental measurement setup consists of a sensor box mounted on a van. The vehicle performs regular trips in Germany's state of North Rhine-Westphalia (NRW) starting in March 2021. The travel time is more than 73 h, 150 000 observations, and a 3422 km covered distance.

Each observation consists of the outputs from GPS, a magnetic compass, acoustic wind, and irradiance sensors. The average sensor read-out frequency is 0.58 Hz. We collect data from different temperature sensors. For instance, apart from the wind speed, the acoustic wind sensor reads the temperature of the air passing through it. In contrast, the irradiance sensor measures the temperature of the sensors' reference module. Our sensor box also features several bearing measurements, namely, GPS and a magnetic compass. The GPS sensor course is accurate at high speeds, whereas the magnetic compass complements the GPS at lower speeds. The raw output of the magnetic sensor is calibrated in the postprocessing stage.

The box is powered via the car battery; hence, it does not record when the engine is off. Therefore, our data contain travel data without observations while the vehicle is parked.

Our sensor box is not unique, and several sensor boxes have been proposed in the literature. Solarjinie^[23] is a sensor box that operates from a battery or external solar panels and records irradiance data at a maximum of 0.06 Hz. Unlike our sensor box, it is compact and can work autonomously without external power. Therefore, it can also collect data when the car's engine is off. However, the device only records GPS location and irradiance, whereas our data provide a more accurate car orientation, two different temperature sources, and wind speed. The temperature and wind values are crucial in yield modeling. Furthermore, our recording rate is 10 times higher.

Another project, PV2Go,^[24] distributes sensor boxes among volunteers and collects data from 50 different vehicles since October 2021. The precise characteristics of the device are unknown, but from the device's description, it seems to record only GPS and irradiance. The data from this project will provide a broader range of driving profiles. Akin to Solarjinie, the PV2Go box is compact and can be mounted by any volunteer without sacrificing the looks of volunteers' cars.

Araki et al.^[14] also performed experimental measurements on a vehicle using five pyranometers. Their data are taken at

approximately 1 Hz, totaling 200 h of driving and 3200 h of parked time. We conjecture that their setup also records irradiance sensor temperature. Regarding the irradiance sensor directions, unlike Araki et al.,^[14] our sensor box does not measure toward the front of the vehicle. Unfortunately, the dataset in Araki et al.^[14] has not been provided in the public domain.

Compared to PV2Go and Solarjinie devices, our setup is bulkier. However, we store a wider variety of data that can benefit yield modeling. The design in Araki et al.^[14] is similar to ours but can record during the vehicle's parked state. However, Araki et al.^[14] lack acoustic wind sensors.

Hereafter, we elaborate on our sensors setup (Section 2.1) and describe the collected data (Section 2.2).

2.1. Sensors Setup

Our sensor setup consists of a data logger box with four irradiance sensors and one acoustic wind sensor. The data logger is implemented with Raspberry PI model 3 b+, powered by the car's electrical system, and records data on an SD card. The data logger and the sensors are mounted on aluminum profiles, attached to a standard roof rack.

The GPS sensor is placed on a data logger box and provides information on the time, location, altitude, speed, and bearing. We use the Adafruit 2324 GPS Hat for the Raspberry PI. In addition, an Adafruit magnetometer (LSM303) complements the GPS-based course.

The magnetometer bearing of the car will generally be less accurate and more prone to distortions than the GPS bearing, provided the vehicle has a sufficient velocity to compute a precise direction. The magnetometer is thus only required to determine the bearing at low speeds. A magnetometer generally needs to be calibrated to compensate for hard and soft magnetic offsets. Most time, our car is moving sufficiently fast to compute a GPS bearing; we calibrate the hard and soft magnetic offsets to match the GPS bearing. After calibration, the overall root-mean-square deviation between the magnetometer and GPS bearings equals 7.4°.

We use four calibrated silicon irradiance sensors from Ingenieurbüro Mencke & Tegtmeier GmbH, of type Si-RS485TC-T-MB. The sensors measure instantaneous irradiance, not the integrated irradiation between measurements.

Irradiance sensors also provide a temperature of the sensor solar reference cell.

The irradiance sensors are mounted on the vehicle's roof and positioned on four sides: roof, left, right, and rear. The roof sensor is oriented toward the sky, and others are oriented toward the horizon. Unfortunately, our specific car setup does not allow placing the rear sensor far behind the roof. Hence, it is exposed to reflections from the car roof. The collected data and our simulation models illustrate this. Furthermore, we suggest that it is essential to periodically clean the irradiance sensor, as they get dusty, especially during the autumn and winter.

We use an FT205EV acoustic wind sensor by FT Technologies Ltd. for measuring wind velocity. The sensor is positioned at approximately the level of the irradiance sensors. In addition to the wind speed and direction (relative to the car), it also provides the acoustic air temperature derived from the measured sound's speed.

Figure 1 shows a photograph of our sensor box setup.

2.2. Collected Data

The data are collected continuously from March 2021. Figure 2 depicts the driving profile between March 2021 and October 2021. The vehicle travels through urban areas in Aachen, Jülich, and Düren, as well as areas with agricultural fields, forests, and the hilly regions in Eifel. The road types range from narrow roads and motorways.

Our vehicle travels in total 3422 km. Throughout the 8 months, the car takes various routes with a total length of 330 km. The total travel time equals 73 h. Most trips start around 8 am from the research center and go toward one of the destination locations. Most of the destinations are located in the southwest direction. The return trips happen between 1 and 3 pm in the northern direction. Such a regular travel pattern introduces an asymmetry in irradiation of the vehicle's left and right sides (see Table 3 in Section 4).

We publish the collected data in a challenge form refs. [28,29]. The challenge contains our sensor measurement data and the satellite-based atmospheric irradiation values (see Section 3.2). Approximately 70% of the data are entirely open, and the rest of the data irradiance sensor outputs are blinded and only used for evaluation. Such an approach permits an honest comparison



Figure 1. View on the sensor box from the rear-right side of the vehicle. The data logger is encapsulated in a weather-proof box and mounted with other sensors on aluminum profiles. The acoustic wind sensor is located right next to the right irradiance sensor. The rear sensor sees many reflections from the white roof of the vehicle.

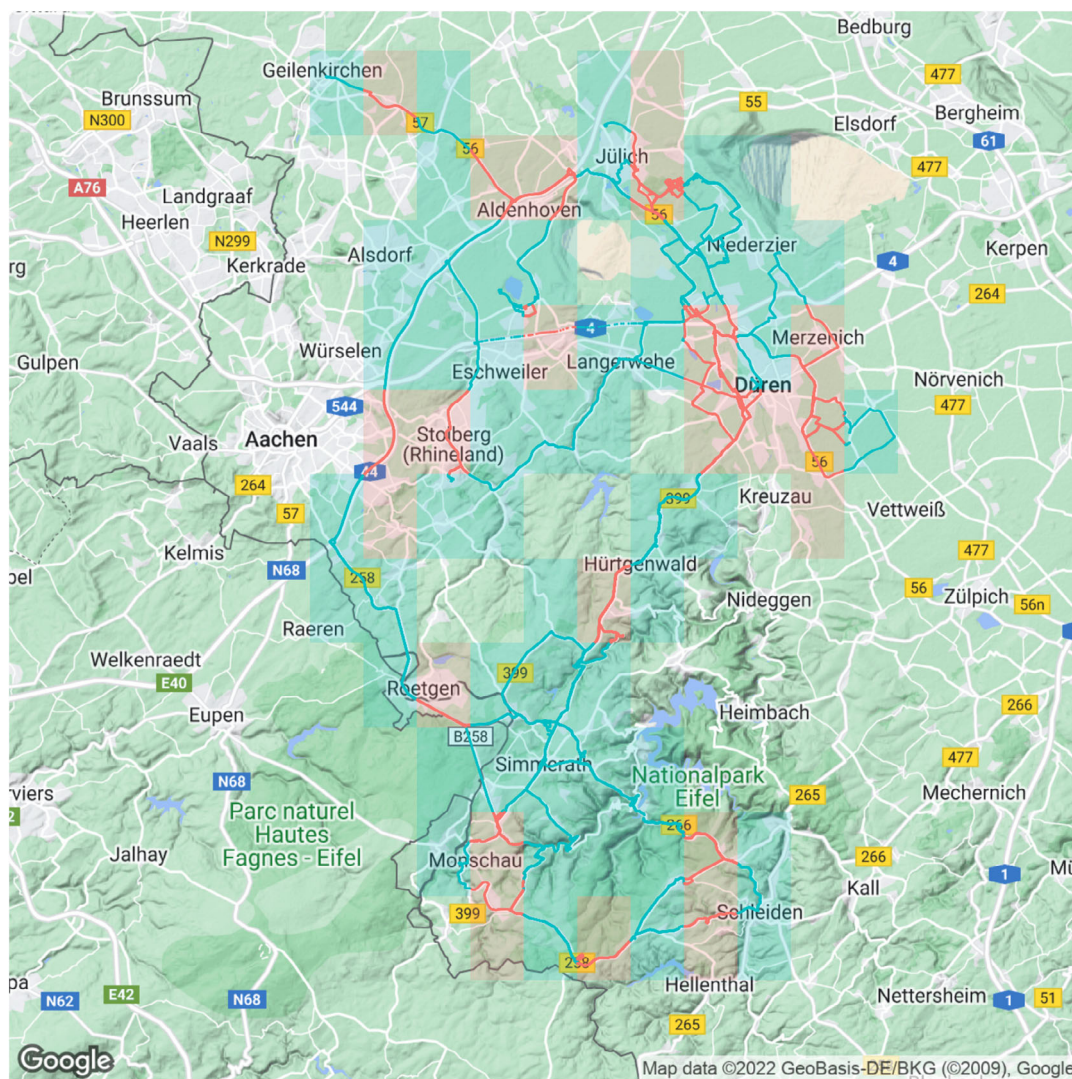


Figure 2. March 2021–October 2021 driving profile. Different colors indicate training (blue) and testing (red) regions. Blue and red points (curves) show the vehicle's movement. The semitransparent blue and red rectangles show the grid used for public and blinded datasets.

of different models and allows other research groups to benchmark their irradiance models. Furthermore, the challenge platform permits additional stages when new data become available.

To evaluate the challenge honestly, we ensure that data in the training and evaluation part of the dataset do not correlate. We achieve this by placing training and evaluation data away from each other. We define a list of regions (sized $3 \times 5 \text{ km}^2$) and randomly allocate some regions to be public and some to be hidden. Approximately 70% of those areas are made public. Figure 2 depicts those regions using blue- and red-colored rectangles.

Table 1 summarizes information on the provided fields and their units.

3. Irradiance Modeling

Our irradiance modeling uses low- and high-resolution topography and low-resolution weather data to compute effective

irradiation on the surface of the moving vehicle. Our approach is implemented through the open-source SSDP^[25] library and PV-GRIP^[27] distributed-computing framework.

Several irradiance modeling approaches have been proposed in the literature. For example, previous studies^[14,19] model solar irradiance by a random distribution of shading objects and car orientation with the correction of the curved surface of the PV modules. The limitation of the modeling approach of Araki et al.^[14] is that their model relies on the random number and assumes that every parameter affecting the solar resource on the car roof and car side is distributed by a simple rule, for example, ranged uniform distribution. Such modeling may be meaningful for the averaged or integrated energy yield. However, it is inapplicable for power prediction in specific driving points, climates, and conditions. The given distributions may not equal the actual situation that varies for every position and time. Hence, the approach is to be applied to annual or other long-term integration like yearly energy yield.

Table 1. Description of fields of the published data.^[28,29]

Field	Description
"gps time utc"	Unix timestamp
"timestr"	Time string in the format "%Y-%m-%d_%H:%M:%S" with UTC time zone (reformatted "gps time utc")
"latitude", "longitude"	GPS coordinates
"gps altitude (m)", "gps speed (m s ⁻¹)", "gps course (deg)", "gps climb (m min ⁻¹)"	Altitude, speed, bearing and climb rate
"gps EPX Estimated * Error"	GPS estimated errors
"Magnetic Bearing [deg.], Magnetic Tilt [deg.]"	Magnetic compass bearing and tilt
"module", "sensor_azimuth", "sensor_zenith"	Side of the irradiance sensor ("module" attains values: "roof", "left", "right", "rear"). "sensor_azimuth" and "sensor_zenith" define orientation of the irradiance sensor. Azimuth computed from magnetic compass, zenith 0 corresponds to the sky orientation
"irradiance_Wm2"	Irradiance sensor readings
"GHI", "DHI", "Clear sky GHI", "Clear sky DHI"	Copernicus irradiance values
"geohash"	Region id which is used in training dataset split ^[40]

Another group^[21,22] uses the "Area Solar Radiation" function in the proprietary software ArcGIS to perform various VIPV-related computations. Brito et al.^[22] query parking site locations using OpenStreetMaps data and raster images obtained by LIDAR point clouds to model irradiation of the parking spaces in Lisbon, Portugal. Their model considers ground declination and shadows cast by the surrounding buildings. They, however, ignore any locations that contain any trees. Furthermore, they neglect the vehicle's height, i.e., their irradiation measurements are simulated at the ground level. Brito et al.^[22] use topography with a resolution of 1 m² pixel⁻¹. Finally, simulations in Brito et al.^[22] are yet to be verified with experimental measurement data.

De Jong et al.^[20] implement an irradiance model based on the Perez All-Weather sky model and the digital surface topography data. They use the nearest weather station to obtain the hourly GHI irradiance values for the irradiance data. For the topography data, they used sampled LIDAR data with the maximum statistic with a resolution of 0.5 × 0.5 m². Their irradiance model is akin to ours but implemented in MATLAB. Their measurement data record the PV module's voltage and current at a rate of 0.0017 Hz, location, orientation, ambient temperature, and wind speed. de Jong and Ziar^[20] verify their model using the PV module power output, which includes not only irradiance but also the influence of the module's temperature.

In the following, we address two questions. First, Section 3.1 elaborates on the SSDP library. Our current model is not ideal, and we discuss its limitations. Then, Section 3.2 discusses the geospatial data we use for our simulation and the challenges it imposes.

3.1. Modeling with SSDP

Various methods exist to model irradiance that considers shading from the environment, ranging from ray-tracing solutions to simpler models such as "r.sun"^[30] and "Solar Analyst".^[31] A complete ray-tracing solution is too computationally intensive for the VIPV setting. However, the simpler models typically use an isotropic diffuse light approximation and are not optimized for VIPV applications. The SSDP library^[25] implements

the Perez All-Weather sky model^[32] to account for a nonisotropic diffuse light component. Furthermore, the SSDP tool implements several VIPV-specific simulation modes to model irradiance along a route, where the orientation and tilt of the incident plane are adapted to the course, road tilt, module orientation, and height offset.

Our irradiance model implementation is similar to the one described in Fu and Rich.^[31] For that, we divide the sky dome into patches and assign an irradiance value for each patch according to the Perez model.^[32] The sun is modeled as a point in the sky. The FreeSPA library^[33] is our open-source implementation of the NREL Solar Position Algorithm.^[34]

The sky is projected on a surface with a given position and orientation, yielding the plane of array irradiance, I_{PoA} , for each observation point. The I_{PoA} consists of several components

$$I_{PoA} = I_{direct} + I_{diffused} + I_{ground} \quad (1)$$

where I_{direct} is the direct light from the sun, $I_{diffused}$ is the diffused light, and I_{ground} is the light that comes from the ground. The I_{direct} is nonzero when the sun is visible to the observer, and is determined using observer orientation, sun position, and the horizon around the observer. The $I_{diffused}$ light consists of all visible sky patches and results from the sky model. The ground component I_{ground} has a simplified model of the light reflected from the ground. We take the light from sky patches obstructed by the horizon and scale the resulting value with the albedo parameter [0,1]. We refer the reader to refs. [31,32] for more details. Our implementation can be obtained here.^[25]

SSDP works with topography data represented either with a raster image (e.g., Digital Elevation Model) or an irregular mesh of points (unprocessed LIDAR point clouds). The library does not use any specific coordinate system. Hence, we resample topography data in a metric coordinate system and feed it to the SSDP. Furthermore, it allows us to sample topography, take tilts in roads, and specify the offset and orientation of modules to model the module position correctly.

The SSDP irradiance model has its limitations. The topography is modeled as a surface and does not capture any 3D objects. For

instance, in our model, trees cast more shadows than in reality. Furthermore, SSDP is not a ray-tracing library; hence, the light reflections are modeled with significant simplifications. Nevertheless, such an approach dramatically improves the performance of simulations, allowing VIPV modeling over long routes.

3.2. Geospatial Data

The dynamic nature of a moving vehicle is the main challenge in the irradiance modeling that distinguishes VIPV from other PV applications. When a car moves, the environment and shading conditions are highly dynamic. Therefore, unlike the problem of irradiation modeling for building-integrated PV, VIPV requires intensive topographical LIDAR data processing. For example, our vehicle covers over 330 km of the unique road surface. Therefore, we must resample and prepare large volumes of data for the SSDP library's input. We developed a scalable distributed-computing framework implemented in the PV-GRIP tool to accelerate this process. We refer the reader to Sovetkin et al.^[26] for more details about the PV-GRIP architecture.

We need two kinds of geospatial data for our simulations: topographical data and atmospheric irradiation data. We use data from three sources for topography data: aerial-measured LIDAR data provided by the NRW state,^[35] satellite-measured Shuttle radar topography data (SRTM),^[36] and Advanced Spaceborne Thermal Emission and Reflection Radiometer (ASTER).^[37] We resample the topography data in the local UTM metric coordinate system to ensure that our shadows are simulated with the correct size.

The LIDAR data are provided in a “laz” format, and we resample the cloud points by computing different statistics for every region of size $30 \times 30 \text{ m}^2 \text{ pixel}^{-1}$. Among those statistics for us are interesting maximum and minimum statistics. **Figure 3** demonstrates the so-called “hillshade” images of the sampled LIDAR data. The left image in **Figure 3** is generated using the maximum value statistic that captures the shape of vegetation and buildings. The minimum value statistic (the right image, **Figure 3**) gives a view with buildings but without trees. The foliage is not visible in the minimum statistic plot since one of the reflections of the laser comes from the ground.

In addition to aerial-measured LIDAR, we use SRTM and ASTER data, the satellite-based topography data. These data sources have a courser resolution of $90 \times 90 \text{ m}^2 \text{ pixel}^{-1}$ and

$30 \times 30 \text{ m}^2 \text{ pixel}^{-1}$ for SRTM and ASTER data, respectively. The satellite-based topography data do not capture any building or vegetation but provide a generic topography outlook.

In addition to the topography data, we use Copernicus,^[38] a satellite-based atmospheric data service. It provides GHI, DHI, and corresponding clear sky values with a spatial resolution of approximately 5 km and temporal resolution of about 10 min.

4. Results

For simulations in this article, we look at the model's performance implemented in the SSDP library using different topography sources: LIDAR, ASTER, and SRTM (see Section 3.2). These data sources are resampled with different resolutions. Furthermore, for each observation data point, the topography raster data are sampled so that a square of a specific size with the center at the observation point is wholly contained inside the sampled raster image. We call this square a minimal square. This sampling strategy ensures that at least the minimal-square-size worth of topography data is used to compute shading.

We sample the LIDAR data with $30 \times 30 \text{ m}^2 \text{ pixel}^{-1}$ resolution, maximum and minimum statistics, and a minimal square size of 200 m. Next, the ASTER data are sampled with a resolution of $10 \times 10 \text{ m}^2 \text{ pixel}^{-1}$ and a minimal square size of 500 m. Finally, the SRTM is sampled with $50 \times 50 \text{ m}^2 \text{ pixel}^{-1}$ and a minimal square size of 2000 m.

Figure 4 shows simulated versus measured irradiance of the roof sensor for each car's location (left) and 1 min average (right). We use LIDAR-max topography data for those simulations with an albedo value of 0.25 and a height offset of 2 m. Unfortunately, many measurements do not agree with simulations (**Figure 4**, left). The modeling errors can be attributed to two sources. First, the limitations of the SSDP discussed in Section 3.1 result in an imprecise representation of geographical objects and their shadows. In particular, our topography simplification produces significantly larger shadows for trees. Second, our model does not include any shading from the clouds, as we use low-resolution satellite-based atmospheric irradiation data to generate the sky model approximation with the Perez All-Weather sky model.

Those modeling errors depend on the vehicle's location and surroundings. **Figure 5** illustrates this by plotting the standard

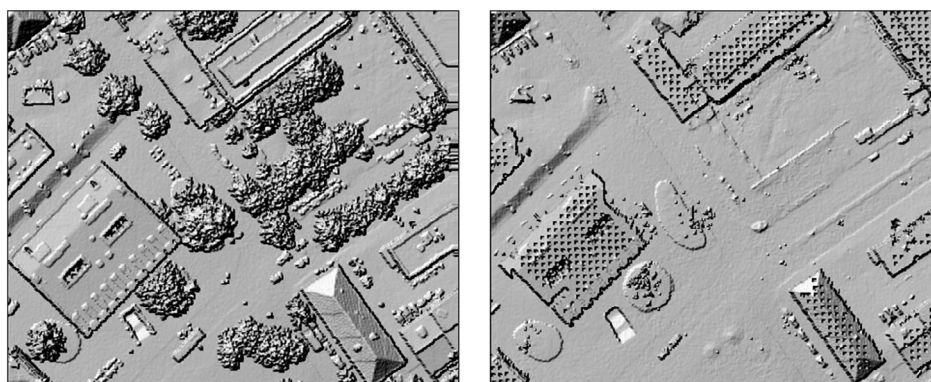


Figure 3. “Hillshade” visualization of terrain sample from LIDAR in the region of the “Super C” building in Aachen, sampled with the maximum statistic (left) and the minimum statistic (right). Resolution $30 \times 30 \text{ m}^2 \text{ pixel}^{-1}$.

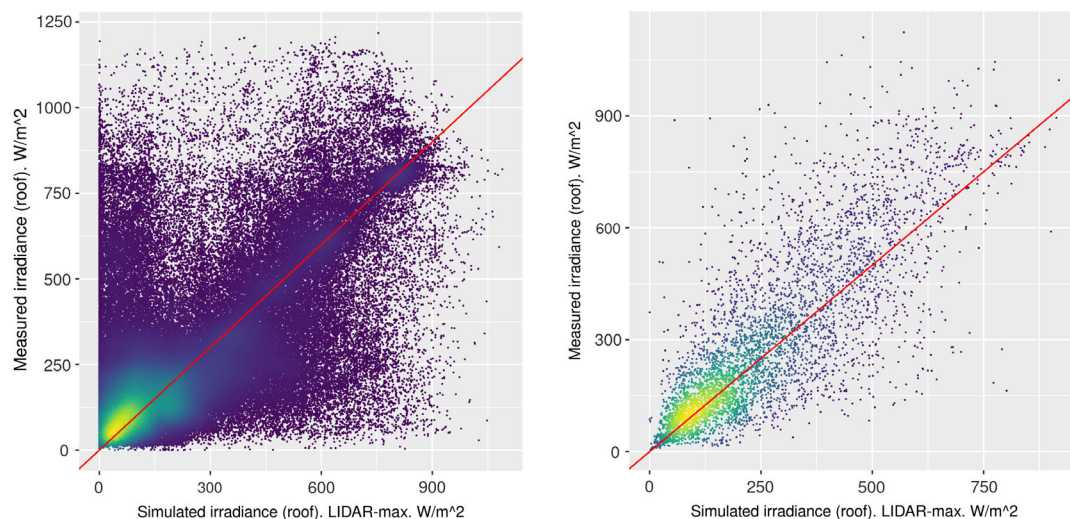


Figure 4. Simulated versus measured irradiance for every observation (left) and average irradiance over 1 min (right) for the roof sensor. The 1 min intervals contain ≈ 35 observations. Bright colors indicate a denser point population. The R^2 value equals 0.37 (left) and 0.63 (right). The bias (measured minus simulated) equals 33 W m^{-2} .

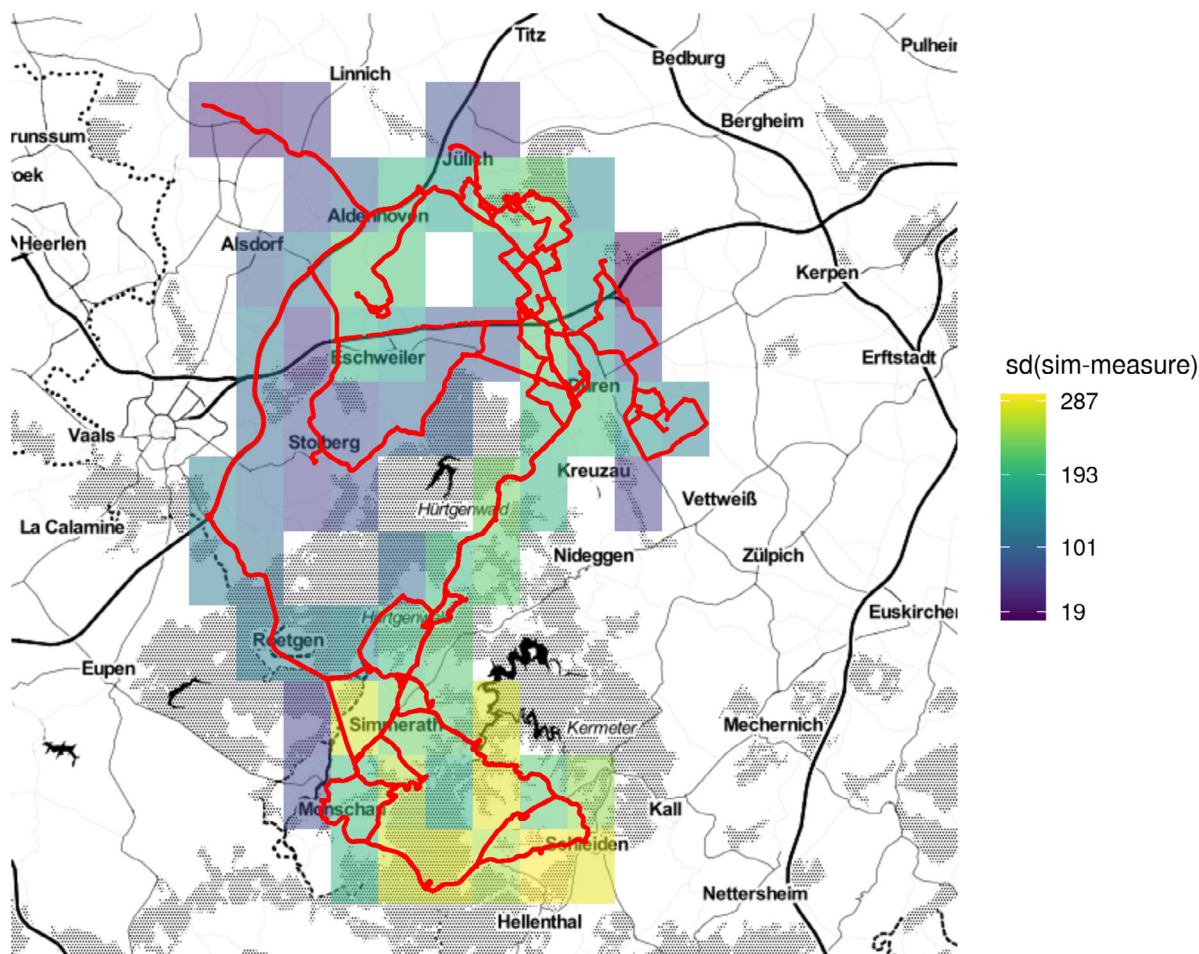


Figure 5. Color squares depict the standard deviation of the difference between simulations and measurements computed for different regions. The red color points correspond to the vehicle locations. The model is less accurate in the southern part: a national park with many forests; and more accurate in the northern region: flat roads surrounded by fields.

deviation between measured and simulated irradiance computed for different travel regions. The brighter colors indicate more significant simulation errors and are located in the southern part. Those are the areas of the national park Eifel with narrow roads that go through forests. The darker colors are primarily located in central and northern areas, where vehicles travel on motorways surrounded by agricultural fields.

The modeling errors do not permit us to have a precise irradiance model for each location. Nevertheless, our model is valid in a statistical sense: when we average irradiance over a short time (Figure 4, right), the model's errors cancel each other, and prediction improves. This improvement is illustrated in Figure 4, where the R^2 value increases from 0.37 (Figure 4, left) to 0.63 (Figure 4, right).

Figure 4 right reveals a slight bias—our model slightly underestimates the irradiance (bias equals 33 W m^{-2}). Such underestimation can be attributed to the LIDAR-max topography because it models opaque trees with more prominent shadows. Simulations with the LIDAR-min topography show a similar $R^2 = 0.65$ for the 1 min average irradiance and a negative bias of -24 W m^{-2} . The LIDAR-min does not contain any tree crowns (see Figure 3, right), so our model overestimates the irradiance.

There are several model parameters that influence the simulation outcome. To illustrate the effect of different parameters, we compute the irradiation of the sensors over the whole measurement period. For that, we integrate irradiance, assuming the irradiance to be constant between measurements, and split all data into parts; there are no observations with a time difference of more than 30 s in every part of the data. Integrated parts are then summed up. The total integration time equals 73 h.

The height offset parameter defines the location height where irradiance is simulated. The left side of Table 2 illustrates that irradiation simulations on the ground-level lead to a 16% irradiation reduction (average for all sensors) compared to the simulations at the 2 m level. Such reduction occurs because shadows are more prominent at the ground level. The albedo parameter controls the amount of ground irradiance component (see Section 3.1). The right side of Table 2 shows simulations for different sensor, albedo values, and height offset of 2 m. The albedo value has a negligible effect on the roof sensor (only little topography is visible from roof sensor orientation) and a significant effect on the sensors oriented toward the horizon. Finally, the number of sky patches may influence the shape of shadows but has a minor influence on the irradiance. In all our

Table 2. Comparison of irradiation (kWh m^{-2}) simulations for different albedo and height offset parameters. All simulations use LIDAR-max topography. The rear sensor needs larger albedo values, as it is exposed to the reflections from the white roof (see Figure 1).

Albedo	0.5		0	0.25	0.5	0.75	1	Measured
Offset	0	1	2					
Roof	17.55	18.90	19.15	19.43	19.71	19.99	20.27	21.85
Left	10.69	12.25	9.48	11.27	13.07	14.87	16.67	12.00
Right	7.83	8.99	6.17	7.86	9.55	11.23	12.92	7.33
Rear	10.23	11.62	8.75	10.52	12.29	14.06	15.83	14.58

Table 3. Comparison of irradiation (kWh m^{-2}) simulations for different topography sources. For those simulations, we select albedo 0.25 for the roof, left and right sensors, and 0.75 for the rear sensor. The height offset parameter is set to 2 m.

	Measured	LIDAR-max	LIDAR-min	ASTER	SRTM	GHI
Roof	21.85	19.43	23.64	27.19	27.54	27.95
Left	12.00	11.27	13.80	16.86	17.26	
Right	7.33	7.86	9.16	11.55	11.79	
Rear	14.58	14.06	16.67	20.10	20.47	
Total	55.76	52.62	63.27	75.70	77.06	

simulations, we selected 269 sky patches. RMSE between irradiance simulation with 1139 and 269 patches equals 12.

Table 3 provides simulation results using different topography data sources. For these simulations, we choose the height offset of 2 m (the van's height). For the left, right, and roof sensors, the albedo value equals 0.25, and for the rear sensor, albedo equals 0.75 (the rear sensor is exposed to the reflections from the white roof, see Figure 1). Different topography data sources allow us to study the influence of various topographical features on irradiation. From Table 3, comparing "LIDAR min" and "measured", we conclude that vegetation decreases irradiation by 13%. Furthermore, vegetation and buildings reduce irradiation by 35% (comparing "measured" with "ASTER" simulations).

Our simulations have been performed on eight heterogeneous nodes with 160 GB of RAM and 52 workers combined. Our dataset of 3422 km of the route takes around 4 h to sample 400 km² of LIDAR data and perform irradiance simulations. LIDAR data sampling takes approximately 3 h. In PV-GRIP, the results of all computation routines are cached; therefore, irradiance simulation in the same region will be computed faster when sampled LIDAR data is available. The performance bottleneck in our simulations are input/output operations, as irradiance simulations take 10 s for a single raster image of 0.4 km² with resolution of a $30 \times 30 \text{ cm}^2 \text{ pixel}^{-1}$. Sampling and simulation for SRTM and ASTER topography data are faster and require approximately 30 min. We use 660 GB for raw data and 200 GB for sampled data in terms of storage.

5. Conclusions

This article introduced a public dataset containing VIPV measurement data. The dataset is published as a challenge,^[28,29] where everyone may benchmark their irradiance model. Generally, VIPV irradiance modeling introduces technical challenges: analyzing the environment around a moving vehicle requires processing a large amount of geospatial data. We overcome this challenge by introducing a distributed-computing-based modeling tool PV-GRIP. Furthermore, irradiance modeling is achieved using our open-source C-library SSDP, which efficiently performs simulations over long routes.

Our irradiance modeling uses high-resolution aerial-measured LIDAR topography and satellite-based low-resolution atmospheric irradiance data. We demonstrated that the topography and sky model approximations do not permit accurate irradiance simulation. Therefore, we recommend utilizing several

sources of topography data to correct for such environmental effects for future work. Nevertheless, we showed that the irradiation model over long periods agrees with the collected measurements.

Acknowledgements

The authors gratefully acknowledge the Helmholtz Data Federation (HDF) for funding this work by providing services and computing time on the HDF Cloud cluster at the Jülich Supercomputing Centre (JSC).^[39] This work was supported by the HGF project “Living Lab Energy Campus (LLEC)”, as well as the “Street” project (Street—Einsatz von hocheffizienten Solarzellen in elektrisch betriebenen Nutzfahrzeugen, Förderkennzeichen: 0324275A). Thanks to the IBG-3 (FZJ) for providing the vehicle and collecting the data.

Open Access funding enabled and organized by Projekt DEAL.

Conflict of Interest

The authors declare no conflict of interest.

Data Availability Statement

The data that support the findings of this study are openly available in [Vehicle measured irradiance data] at [https://doi.org/10.34730/3c8732aca9e3423aad57af2bba3a1dea], reference number [28,29].

Keywords

geospatial data, measurement data, vehicle-integrated PV

Received: June 30, 2022

Revised: October 5, 2022

Published online: October 27, 2022

- [1] A. K. Shukla, K. Sudhakar, P. Baredar, *Energy Build.* **2017**, *140*, 188.
- [2] S. R. Wadhawan, J. M. Pearce, *Renewable Sustainable Energy Rev.* **2017**, *80*, 125.
- [3] B. Commault, T. Duigou, V. Maneval, J. Gaume, F. Chabuel, E. Voroshazi, *Appl. Sci.* **2021**, *11*, 11598.
- [4] Lightyear company, lightyear.one/company/ (accessed: October 2022).
- [5] Sono motors, sonomotors.com/en/sion/ (accessed: October 2022).
- [6] O. Kanz, A. Reinders, J. May, K. Ding, *Energies* **2020**, *13*, 5120.
- [7] M. Heinrich, C. Kutter, F. Basler, M. Mittag, L. E. Alanis, D. Eberlein, A. Schmid, C. Reise, T. Kroyer, D. H. Neuhaus, in *Proc. of the 37th European Photovoltaic Solar Energy Conf. and Exhibition*, Lisbon, Portugal, **2020**, pp. 1695–1700.
- [8] A. Sierra, A. Reinders, *Prog. Photovoltaics: Res. Appl.* **2021**, *29*, 802.
- [9] M. Yamaguchi, T. Masuda, K. Araki, D. Sato, K.-H. Lee, N. Kojima, T. Takamoto, K. Okumura, A. Satou, K. Yamada, T. Nakado, Y. Zushi, M. Yamazaki, H. Yamada, *Energy Power Eng.* **2020**, *12*, 375.
- [10] M. Yamaguchi, K. Nakamura, R. Ozaki, N. Kojima, Y. Ohshita, T. Masuda, K. Okumura, A. Satou, T. Nakado, K. Yamada, T. Tanimoto, Y. Zushi, T. Takamoto, K. Araki, Y. Ota, K. Nishioka, *Solar RRL* **2022**, 2200556, https://doi.org/10.1002/solr.202200556.
- [11] C. Thiel, A. G. Amillo, A. Tansini, A. Tsakalidis, G. Fontaras, E. Dunlop, N. Taylor, A. Jäger-Waldau, K. Araki, K. Nishioka, *Renewable Sustainable Energy Rev.* **2022**, *158*, 112109.
- [12] R. Peibst, H. Fischer, M. Brunner, A. Schießl, S. Wöhe, R. Wecker, F. Haase, H. Schulte-Huxel, S. Blankemeyer, M. Köntges, *Sol. RRL* **2022**, *6*, 2100516.
- [13] S. Neven-du Mont, M. Heinrich, A. Pfreundt, C. Kutter, A. Tummalieh, H. Neuhaus, in *Proc. of the 37th European Photovoltaic Solar Energy Conf. and Exhibition*, online, Lisbon, Portugal **2020**, pp. 822–827.
- [14] K. Araki, Y. Ota, M. Yamaguchi, *Appl. Sci.* **2020**, *10*, 872.
- [15] Y. Ota, K. Araki, A. Nagaoka, K. Nishioka, *Prog. Photovoltaics: Res. Appl.* **2022**, *30*, 152.
- [16] M. Kolhe, S. Adhikari, T. Muneer, *Appl. Energy* **2019**, *233*, 403.
- [17] Y. Tomita, Y. Nagai, M. Saito, N. Niina, Y. Zushi, in *2019 8th Int. Conf. on Renewable Energy Research and Applications (ICRERA)*, IEEE, Piscataway, NJ **2019**, pp. 527–533.
- [18] G. Wetzel, L. Salomon, J. Krügener, D. Bredemeier, R. Peibst, *Prog. Photovoltaics: Res. Appl.* **2022**, *30*, 543.
- [19] K. Araki, K.-H. Lee, T. Masuda, Y. Hayakawa, N. Yamada, Y. Ota, M. Yamaguchi, in *2019 IEEE 46th Photovoltaic Specialists Conference (PVSC)*, IEEE, Piscataway, NJ **2019**, pp. 1218–1225.
- [20] D. De Jong, H. Ziar, *Sol. RRL* **2022**, 2200642, https://doi.org/10.1002/solr.202200642.
- [21] T. Santos, N. Gomes, S. Freire, M. Brito, L. Santos, J. Tenedório, *Appl. Geogr.* **2014**, *51*, 48.
- [22] M. C. Brito, T. Santos, F. Moura, D. Pera, J. Rocha, *Transp. Res. Part D: Transp. Environ.* **2021**, *94*, 102810.
- [23] Solarjinie VIPV irradiance logger, enerjin.com/Solarjinie_VIPV_1p0_spec_sheet.pdf, (accessed: October 2022).
- [24] PV2Go: solar potential for vehicles, pv2go.org/, (accessed: October 2022).
- [25] SSDP: Simple Sky Dome Projector, github.com/IEK-5/SSDP, (accessed: October 2022).
- [26] E. Sovetkin, N. Patel, A. Gerber, B. E. Pieters, in *Proc. of the 38th European Photovoltaic Solar Energy Conf. and Exhibition*, online **2021**, pp. 1152–1160.
- [27] PV-GRIP: PV Geographic Raster Image Processor, github.com/IEK-5/PV-GRIP, (accessed: October 2022).
- [28] VIPV irradiation modelling challenge, helmholtz-data-challenges.de/web/challenges/challenge-page/94/overview, (accessed: October 2022).
- [29] Data for VIPV challenge, https://doi.org/10.34730/3c8732aca9e3423aad57af2bba3a1dea, (accessed: October 2022).
- [30] M. Šúri, J. Hofierka, *Trans. GIS* **2004**, *8*, 175.
- [31] P. Fu, P. M. Rich, In *Proc. of the 19th Annual ESRI User Conf.*, San Diego, USA, **1999**.
- [32] R. Perez, R. Seals, J. Michalsky, *Sol. Energy* **1993**, *50*, 235.
- [33] FreeSPA: free implementation of NREL SPA, github.com/IEK-5/freespa, (accessed: October 2022).
- [34] I. Reda, A. Andreas, *Sol. Energy* **2004**, *76*, 577.
- [35] 3d-measurement data in North Rhine-Westphalia, bezreg-koeln.nrw.de/brk_internet/geobasis/hoeihenmodelle/3d-messdaten/index.html, (accessed: October 2022).
- [36] Shuttle radar topography data, dds.cr.usgs.gov/srtm/version2_1/, (accessed: October 2022).
- [37] AIST, japan spacesystems, and US/japan ASTER science team, 2009: ASTER global digital elevation model. NASA EOSDIS land processes DAAC, NASA, METI, cmr.earthdata.nasa.gov/search/concepts/C1711961296-LPCLLOUD.html, (accessed: October 2022).
- [38] Copernicus open access hub, scihub.copernicus.eu/, (accessed: October 2022).
- [39] B. Hagemeyer, *J. Large-Scale Res. Facil.* **2019**, *5*, A137.
- [40] Wikipedia: Geohash, en.wikipedia.org/wiki/Geohash, (accessed: October 2022).